



Tropical Transition of Hurricane Chris (2012) over the North Atlantic Ocean: A Multiscale Investigation of Predictability

MICHAEL MAIER-GERBER

Institute of Meteorology and Climate Research, Karlsruhe Institute of Technology, Karlsruhe, Germany

MICHAEL RIEMER

Institute for Atmospheric Physics, Johannes Gutenberg University, Mainz, Germany

ANDREAS H. FINK AND PETER KNIPPERTZ

Institute of Meteorology and Climate Research, Karlsruhe Institute of Technology, Karlsruhe, Germany

ENRICO DI MUZIO

Institute for Atmospheric Physics, Johannes Gutenberg University, Mainz, and Institute of Meteorology and Climate Research, Karlsruhe Institute of Technology, Karlsruhe, Germany


RON MCTAGGART-COWAN

Numerical Weather Prediction Research Section, Environment and Climate Change Canada, Dorval, Quebec, Canada

(Manuscript received 23 May 2018, in final form 1 January 2019)

ABSTRACT

Tropical cyclones that evolve from a nontropical origin and undergo tropical transition (TT) play a prominent role in cyclogenesis in the North Atlantic Ocean. They pose a special challenge for predictions, as they often emerge at the end of a multiscale cascade of atmospheric processes. Here we use operational European Centre for Medium-Range Weather Forecasts ensemble predictions to investigate the TT of North Atlantic Hurricane Chris (2012), whose formation was preceded by the merger of two potential vorticity (PV) maxima, eventually resulting in the cyclone-inducing PV streamer. The principal goal is to elucidate the dynamic and thermodynamic processes governing the predictability of Chris's cyclogenesis and subsequent TT. Dynamic time warping is applied to identify ensemble tracks that are similar to the analysis track. This technique permits small temporal and spatial shifts in the development. The formation of the pre-Chris cyclone is predicted by those members that also predict the merging of the two PV maxima. The PV streamer's shape and its position relative to the pre-Chris cyclone determine whether the cyclone follows the TT pathway. The transitioning cyclones are located inside a favorable region of high equivalent potential temperatures that result from a warm seclusion underneath the cyclonic roll-up of the PV streamer. A systematic investigation of consecutive ensemble forecasts indicates that sudden changes in ensemble statistics of cyclone metrics are linked to specific events. The present case exemplifies how a novel combination of Eulerian and cyclone-relative ensemble forecast analysis tools allow inference of physical causes of abrupt changes in predictability.

 Denotes content that is immediately available upon publication as open access.

 Supplemental information related to this paper is available at the Journals Online website: <https://doi.org/10.1175/MWR-D-18-0188.s1>.

Corresponding author: Michael Maier-Gerber, michael.maier-gerber@kit.edu

1. Introduction

Tropical transition (TT) describes the phenomenon when a tropical cyclone (TC) emerges from an extratropical cyclone (Davis and Bosart 2003, 2004). During TT,



This article is licensed under a [Creative Commons Attribution 4.0 license](http://creativecommons.org/licenses/by/4.0/) (<http://creativecommons.org/licenses/by/4.0/>).

the extratropical cyclone transforms from a cold- to a warm-core system. A cascade of events commonly precedes the TT: anticyclonic wave breaking (e.g., [Thorncroft et al. 1993](#); [Postel and Hitchman 1999](#)) causes an upper-level precursor potential vorticity (PV) trough to penetrate into the (sub)tropics ([Galarneau et al. 2015](#)), which initially induces the development of either an antecedent extratropical ([Davis and Bosart 2004](#)) or subtropical cyclone ([Evans and Guishard 2009](#); [González-Alemán et al. 2015](#); [Bentley et al. 2016, 2017](#)). The interplay between the upper-tropospheric PV trough and a low-level baroclinic zone facilitates the organization of convection embedded ([Davis and Bosart 2004](#); [Hulme and Martin 2009](#)) and is characteristic of a TT event, distinguishing it from other baroclinically influenced pathways of TC genesis. The convection associated with the precursor cyclone eventually diminishes the PV gradients above the cyclone center and, hence, reduces vertical wind shear ([Davis and Bosart 2003, 2004](#)), providing a favorable environment for the cyclone to acquire tropical nature.

TC developments are traditionally classified into “tropical only” and “baroclinically influenced” categories (e.g., [Hess et al. 1995](#); [Elsner et al. 1996](#)). [McTaggart-Cowan et al. \(2008, 2013\)](#) further suggest a more precise classification of TC development pathways based on an analysis of two metrics, which assess baroclinicity in the lower and upper troposphere, respectively. The two most baroclinically influenced categories are identified to represent “weak TT” and “strong TT,” distinguished by the strength of the baroclinicity in the lower troposphere.

From a climatological perspective, [McTaggart-Cowan et al. \(2013\)](#) reveal that merely 16% of all global TCs between 1948 and 2010 resulted from TT, but that the relative importance of the TT development pathway is exceptionally high in the North Atlantic basin (almost 40%). Because of the extratropical origin of the precursor PV troughs, North Atlantic TCs that emerge from a TT generally tend to form at higher latitudes ([Bentley et al. 2016](#)), and reach weaker intensities on average compared to all TCs ([McTaggart-Cowan et al. 2008](#)). However, [Davis and Bosart \(2004\)](#) point out the challenge of accurately forecasting these events, because they primarily occur in proximity to the eastern seaboard of North America ([McTaggart-Cowan et al. 2008](#)).

In a recent study, [Wang et al. \(2018\)](#) examine reforecasts in terms of their skill to predict tropical cyclogenesis in the North Atlantic, using the pathway classification of [McTaggart-Cowan et al. \(2013\)](#). The authors conclude that the two TT categories are less predictable than the others, a finding that they attribute to forecast errors of the deep-layer shear and the moisture in the mid-troposphere. They also speculate that the interactions of precursor features and processes required for TT further

reduce the overall predictability as those constitute additional probability factors that multiplicatively extend the joint probability for non-TT pathways. Despite this probabilistic way of viewing TT predictability, it still remains unclear which factors of uncertainty cause predictability issues (i.e., strikingly rapid changes in forecast uncertainty with lead time) at the different stages of the process. The aim of this study is to fill this gap by identifying (thermo)dynamic causes for such changes in the predictability of (i) the formation of the pre-tropical cyclone, (ii) its TT, and (iii) the structural evolution, in the European Centre for Medium-Range Weather Forecasts (ECMWF) ensemble forecasts of Hurricane Chris (2012) initialized throughout the pre-TT portion of the cyclone’s life cycle.

Hurricane Chris was chosen for this multiscale predictability study because of the complex antecedent PV dynamics and the strong baroclinic environment in the upper and lower levels that facilitated the development of the extratropical precursor cyclone. The cyclone can be unambiguously classified as a “strong TT” case with regard to the climatology of [McTaggart-Cowan et al. \(2013\)](#), and may therefore serve as a suitable archetype for investigation of TT predictability. At lead times greater than 2 days, the model struggles to develop the pre-Chris cyclone; however, a strong increase in the number of ensemble members predicting cyclone formation 2–3 days before its actual development in the analysis means that focus can be shifted to the predictability of TT itself from a structural perspective. Finally, cyclone structure statistics from consecutive ensemble forecasts initialized up to 9 days before TT will allow to link strikingly rapid changes in predictability of structural evolution to antecedent (thermo)dynamic processes. Though individual ensemble forecasts have been examined to assess predictability of cyclone-structural evolution before (e.g., [González-Alemán et al. 2018](#)), the present case study is the first to investigate changes in predictability of TT with lead time and thus contributes to a deeper understanding of the associated sources of uncertainty.

Following this introduction, [section 2](#) will describe the data used and the methods applied in this study. The synoptic overview in [section 3](#) highlights the key atmospheric features that were associated with the TT of Chris, before the results in terms of predictability are presented in [section 4](#). The findings and conclusions from this study are discussed in [section 5](#).

2. Data and methods

a. Data

The present case study is based on gridded, 6-hourly operational analysis and ensemble forecast data from

the ECMWF. To assess the evolution of predictability, consecutive ensemble forecasts initialized at 0000 UTC between 10 June and 19 June 2012—equivalent to 9.5 (7) days prior to the formation of TC Chris (the pre-Chris cyclone)—are systematically investigated. The minimum horizontal grid spacing available for the first 10 days of the ensemble forecasts is 0.25° . To allow for comparison, analysis and ensemble forecasts are analyzed using that resolution. PV fields, however, are only examined on the synoptic scale, and thus analyzed at a coarser resolution of 0.5° .

b. Ensemble partitioning: Cyclone versus no cyclone

In a first step, every ensemble forecast considered in this study is split into “cyclone” and “no-cyclone” groups to elucidate dynamic causes limiting predictability of the pre-Chris cyclone’s formation. The group memberships are determined based on similarity between forecast tracks and the analysis track using a dynamic time warping technique (see section 2c for details). This track-based approach for the identification of equivalent cyclones in the forecast members ensures that those are excluded that are of substantially different origin from the pre-Chris cyclone. An ensemble member thus belongs to the cyclone (no-cyclone) group when it predicts (lacks) such a “similar track.” Group names are italicized hereafter to better distinguish them from text.

c. Cyclone tracking and evaluation of forecast tracks

The simple cyclone tracking algorithm described by Hart (2003) is employed here because its performance compared to manual tracking was found to be acceptable. Based on mean sea level pressure data, this approach successively evaluates 5° squares that partially overlap with their adjacent ones to also consider cyclones at the edges. Three criteria are required to meet for a successful detection of a cyclone center within the square: (i) the minimum central pressure cannot exceed 1020 hPa, (ii) the square must enclose a 2-hPa gradient, and (iii) the center has to be tracked for at least 1 day. Once all time steps of an analysis or forecast are evaluated in terms of cyclone centers in the domain of interest, further conditions are imposed to connect centers to a physically consistent track. These conditions concern the translation speed and changes in the orientation of the track [see Hart (2003) for details]. More sophisticated tracking algorithms that deal with splits and merges (Neu et al. 2013) are not required here because the evolution of the predicted cyclone is relatively simple in the ensemble.

The application of this tracking technique to the analysis data directly yields a track, which is hereafter referred to as the “analysis track.” By contrast, an

objective approach is required to evaluate whether each ensemble member features a track that may be deemed similar to the analysis track. Most studies typically evaluate spatial distances between forecast and analysis tracks, thus making the a priori assumption that forecast errors solely occur in space. However, it may be that a forecast predicts a track accurately in space but slightly shifted in time, for instance because of a lag in the precursor PV dynamics. In the present study, we therefore want to be less restrictive and also allow for small temporal shifts in the forecast tracks, using a dynamic time warping technique. The advantage of this approach is that two tracks of different lengths can be nonlinearly matched with respect in time (Sakoe and Chiba 1978; Berndt and Clifford 1994), thereby taking into account (local) temporal shifts (Chen and Ng 2004). Because this case study has a particular focus on the development phase of Chris, the method is applied to calculate the shortest warp path (d_{DTW}) between each forecast track and the first 48 h of the analysis track after the pre-Chris cyclone had formed (not considering cyclone intensity for track matching). If a forecast was initialized after the starting time of the analysis track, the first 48 h after the initialization are considered instead. Berndt and Clifford (1994) recommend applying a warping window that restricts temporal shifts to ensure reasonable matching. In this case study, forecast tracks are allowed to be locally shifted in time relative to the analysis track by ± 12 h at most. Figure 1 shows an example of how a forecast track can be aligned with the analysis track, and how this case would be transferred to a time warping matrix, representing the spatial distances of all potential warp path segments between the two tracks. Given the time series of cyclone positions of the analysis track $A = (a_0, a_6, \dots, a_{48})$ and the forecast track $F = (f_{-12}, f_{-6}, f_0, \dots, f_{60})$, d_{DTW} can be recursively defined as

$$d_{DTW}(i, j) = \|a_{h_i} - f_{h_j}\| + \min[d_{DTW}(i-1, j-1), d_{DTW}(i-1, j), d_{DTW}(i, j-1)], \quad (1)$$

where the analysis and forecast hours $h_i = 6(i-1)$ and $h_j = 6(j-1)$ are functions of the matrix indices $i = 1, 2, \dots, 9$ and $j = -1, 0, \dots, 11$, respectively. This formulation ensures that the warp path aligns the tracks in a monotonic and continuous manner. In addition to these implicit conditions, another rule is imposed for the boundaries. For forecast tracks that last longer than the first 48 h after the formation of the pre-Chris cyclone in the analysis, the later part is not considered in the calculation of d_{DTW} . The warping path starts with the distance between the first point of the analysis track a_0 and

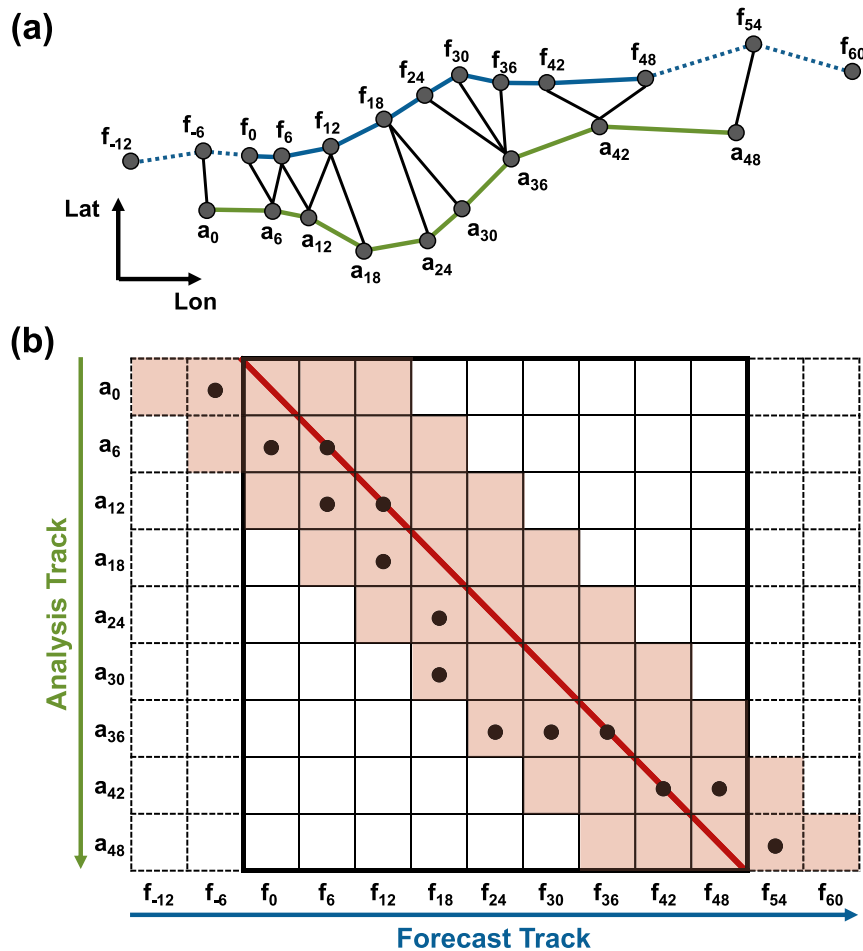


FIG. 1. (a) Illustrative example of a minimized dynamic time warped path between a forecast track (blue trajectory) and the first 48 h of the analysis track after the pre-Chris cyclone had formed (green trajectory). The black lines indicate how the total warp path is composed of individual segments that connect the cyclone positions (gray-filled black circles). (b) Corresponding warping matrix, visualizing how the spatiotemporal similarity is measured. Each matrix element contains a spatial distance between a pair of cyclone positions from the two cyclone tracks, with the minimum value identified by a black dot. Because of a maximum-allowed temporal shifting of ± 12 h in the matching, the warping matrix is extended (dashed arrays). The light red area highlights the warping window in which the shortest warp path (connection of the black dots) is allowed to deviate from the nontemporally shifted matching (red solid line). For more details see section 2c.

the closest forecast track point from f_{-12}, \dots, f_{12} . Following the recursive definition in (1), the calculation of the warp path is continued until the last point of the analysis track a_{48} is aligned with the closest track point of the corresponding forecast subset f_{36}, \dots, f_{60} . These boundary conditions guarantee that the analysis track is compared to the most similar part of the forecast track. To allow for comparison with other tracks, the calculated warp pathlength is then divided by the number of segments to yield the average spatiotemporal discrepancy between forecast and analysis tracks (\overline{d}_{DTW}).

All tracks identified in a given ensemble member m , are compared to the analysis track following the procedure outlined above. The candidate track with the shortest average warp path is treated as the similar track of ensemble member m , provided that \overline{d}_{DTW} does not exceed 700 km. This value was found to be the best choice over a range of thresholds that were tested for all consecutive ensemble forecasts (see Fig. S1 in the online supplemental material). Smaller thresholds tend to be too restrictive, higher ones cause an unrealistic inflation of the number of similar tracks.

d. Cyclone group partitioning: Warmer-core versus colder-core terciles

A further stratification of the *cyclone* group into “warmer-core,” “intermediate-core,” and “colder-core” terciles allows investigation of whether different tendencies in the ensemble prediction of the cyclone’s thermal core structure can be attributed to distinct (thermo)dynamic scenarios. Tercile group names are italicized hereafter to better distinguish them from text. In addition, the application of this partitioning strategy to all ensemble forecasts considered (initializations between 10 and 19 June) is also used to link rapid changes in the predictability of structural evolution with lead time to prominent events in the antecedent (thermo)dynamics. Terciles are technically separated based on the maximum $-V_T^U$ values reached between 0000 UTC 19 June and 0000 UTC 20 June (see section 2e for metric definition) to distinguish between cyclones that barely complete a shallow warm seclusion (Shapiro and Keyser 1990) and TCs that reach the stage of a TC with widespread deep convection. This period of valid times is chosen in preference to a single one to be consistent with the ± 12 -h warping window applied for the dynamic time warping technique (see section 2c). Instead of the tercile-based approach, more sophisticated clustering techniques for trajectories in cyclone phase space (see section 2e) were tested, but had to be rejected, since the resulting clusters either did not separate between distinct physical scenarios, or produced cluster sizes that were too different to proceed with composite analyses.

e. Cyclone phase space

The cyclone phase space metrics developed by Hart (2003) are calculated along each forecasted track to gain insight into the structural evolution of each predicted developing cyclone and to check whether it transitions into a TC. The result is a set of trajectories in the three-dimensional phase space spanned by the lower-tropospheric thickness asymmetry B , the thermal wind in the lower troposphere $-V_T^L$, and the thermal wind in the upper troposphere $-V_T^U$. These three cyclone-relative metrics are derived from geopotential height data within a radius of 500 km. A change in sign of the $-V_T^L$ and/or $-V_T^U$ metrics is indicative of a change in the thermal structure of the cyclone’s core: negative values represent a cold-core system and positive values a warm-core system. Cyclone symmetry is assessed by comparing B to the 10-m threshold derived from a climatological study by Hart (2003). Unlike the original definition of the lower (900–600 hPa) and upper layers (600–300 hPa) by Hart (2003), the alternative separation into 925–700 and

700–400 hPa suggested by Picornell et al. (2014) is used. They argue that these levels are more suitable for higher latitudes because of the lower tropopause height, which is further reduced as the cyclone interacts with the upper-level precursor trough during the pre-tropical phase. In accordance with Hart (2003), a 24-h moving average is applied to obtain smoother trajectories, facilitating the identification of phase transitions.

f. Composite approaches, normalized differences, and statistical significance testing

Applying the partitioning strategies described in sections 2b and 2d, two types of composite approaches are calculated to identify differences between the *cyclone* and *no-cyclone* (*warmer-core* and *colder-core*) subsets. While plain Earth-relative composites (Eulerian perspective) are primarily used to examine the antecedent dynamics on the synoptic scale prior to the formation of the pre-*Chris* cyclone, cyclone-relative composites (cyclone perspective) provide insight into thermodynamics and convective organization on the mesoscale after the pre-*Chris* cyclone forms.

Where absolute values matter (e.g., vertical wind shear), composite means are presented for each subset separately. In most cases, however, it is more convenient to directly analyze and discuss composite differences between the separated subsets. Therefore, similar to a forecast sensitivity study from Torn et al. (2015), normalized differences are computed by subtracting the mean of one subset from the mean of the counterpart subset and subsequently dividing by the ensemble standard deviation to allow for spatial and temporal comparisons. Throughout this paper, statistical significance of composite differences is determined using a bootstrap method with $n = 10\,000$ random draws to resample the unknown underlying probability density functions. For each grid point, it is tested whether the differences are significantly different from zero at the two-sided significance level of 5%. To avoid multiple hypothesis testing, its associated potential for misinterpretations (Wilks 2016), and to preserve spatial and temporal correlation structures, the resampling is only performed once for every combination of partitioning strategy and initialization time (i.e., statistical significance testing is based on the same resampling output for every horizontal grid point, variable, and forecast time).

3. Synoptic overview

This section describes the antecedent synoptic-scale dynamics that led to the formation and subsequent TT of *Chris*, and introduces the key atmospheric features

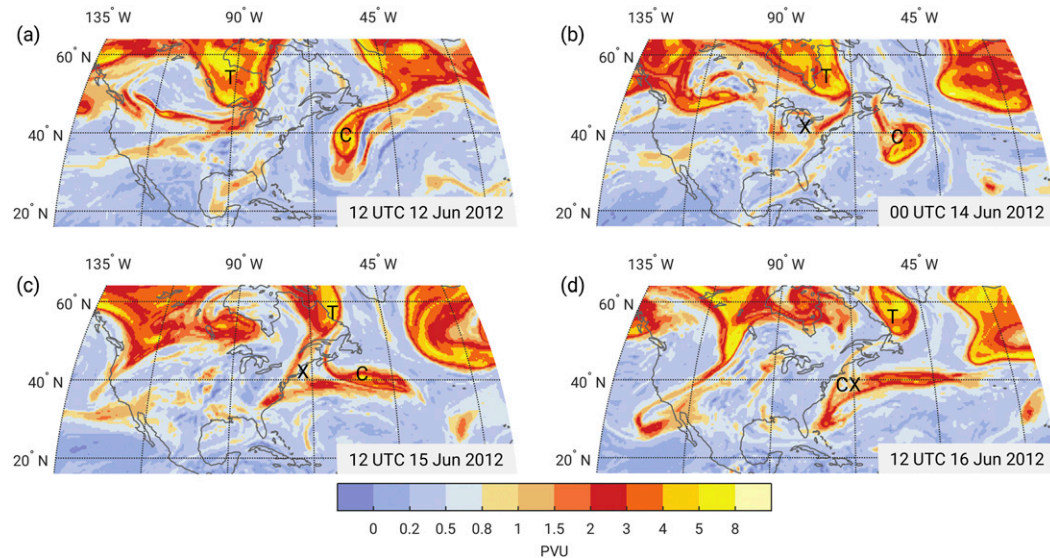


FIG. 2. Upper-level PV development prior to Chris's formation. The 500–250-hPa layer-averaged PV (shaded in PVU, where $1 \text{ PVU} = 10^{-6} \text{ K kg}^{-1} \text{ m}^2 \text{ s}^{-1}$) in the ECMWF analysis valid at (a) 1200 UTC 12 Jun, (b) 0000 UTC 14 Jun, (c) 1200 UTC 15 Jun, and (d) 1200 UTC 16 Jun 2012. The cutoff low, trough, and PV remnants are labeled with C, T, and X, respectively. The merged PV streamer is labeled with CX in (d).

whose predictability will be investigated. In addition, the evolution of the cyclone's structure during TT is discussed using Hart's cyclone phase space.

a. Formation of the precursor trough

The initial trigger for the formation of the precursor trough is anticyclonic wave breaking that takes place over the northwest Atlantic Ocean on 12 June 2012 (Fig. 2a; hereafter all dates are in 2012), which first results in a quasi-stationary, upper-level cutoff low near 40°N , 55°W (labeled C in Figs. 2a,b). In the meantime, the upstream trough (labeled T) reaches the east coast of North America, bringing with it unorganized high-PV air (labeled X) to its south, which is the upper-level remnant of a strong Pacific cyclone that hit the west coast of North America on 9 June (not shown). This PV remnants start to interact and merge with the cutoff low (hereafter “merging”/“merger” always refers to these two PV maxima), forming a zonally oriented PV streamer on 15 June (Fig. 2c). Because this streamer ultimately acts as the precursor trough for Chris, the 15 June PV merger will be studied in detail from a predictability perspective in section 4a. During the subsequent development of the pre-Chris cyclone, the western portion of the equatorward penetrating PV merger begins to roll up cyclonically (16 June, label CX in Fig. 2d).

b. Development of the surface low

A weak surface low, which would later become Chris, develops during the cyclonic roll-up of the upper-level

PV streamer around 0000 UTC 17 June (Fig. 3a). The center of the surface low is located at the leading edge of the PV streamer, east of its southwestern tip. It will be shown below (section 4a) that the shape and position of the PV streamer at this time is another key feature for the predictability of Chris's development. The interaction between the surface low and the upstream trough, leading to a further deformation of the PV streamer, is prominent during Chris's development (Figs. 3a–c). According to the official TC report on Chris from the National Hurricane Center (Stewart 2013), the upper-level PV streamer eventually shears off the cyclone at 1200 UTC 19 June (Fig. 3e) and Chris becomes tropical. Hereafter, we therefore consider this time as the end of TT and the beginning of the tropical phase of Chris's life cycle.

In the lower troposphere, the pre-Chris cyclone develops near an airmass boundary, with its center located in the warm and moist air south of a large equivalent potential temperature (θ_e) gradient (Fig. 3b). The cyclone is steered northeastward along the leading edge of the upper-level PV streamer as it intensifies (Fig. 3c). Over this period, a slot of low- θ_e air wraps cyclonically around the low center (Fig. 3d), a common feature in subtropical cyclones (e.g., Hulme and Martin 2009; Davis and Bosart 2003). Over the next 36 h, the pre-Chris cyclone detaches from the high- θ_e reservoir to its south and east and is then embedded in an area of high- θ_e air surrounded by lower values at radii beyond approximately 350 km (Fig. 3f).

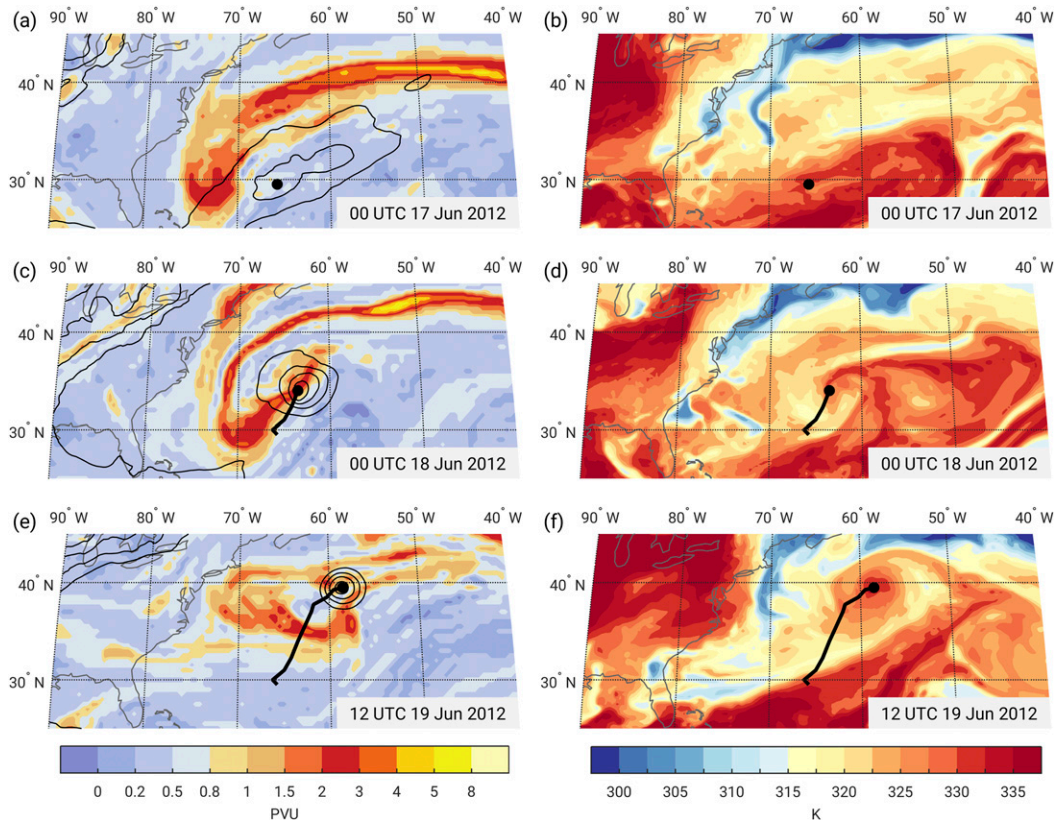


FIG. 3. Upper-level PV and low-level thermal structure during the pretropical phase of Chris. (a),(c),(e) As in Fig. 2. Additionally, MSLP lower than or equal to 1014 hPa (contours, every 2 hPa) for (a) 0000 UTC 17 Jun, (c) 0000 UTC 18 Jun, and (e) 1200 UTC 19 Jun 2012. (b),(d),(f) θ_e at 850 hPa (shaded, K) corresponding to the times of (a),(c),(e). Current cyclone position and past track are denoted by black-filled circles and black lines, respectively.

c. Thermostructural changes before TC development

Early in its life cycle (0000 UTC 17 June), the weak cyclone exhibits a symmetric, cold-core structure (Figs. 4a,b). Subsequently, as the surface low starts to interact with the approaching upper-level trough, a wavelike disturbance on the low-level baroclinic zone (Fig. 3d) causes asymmetric baroclinicity (the B metric) to increase markedly until 0000 UTC 18 June. However, the asymmetric phase ends within 24 h, with the B metric falling below the 10-m threshold when the low-level baroclinic zone changes to a warm seclusion with a well-defined dry slot (Fig. 3f). Over this period of changes in the cyclone-relative symmetry, the core experiences a continuous warming and becomes a symmetric, moderately deep warm core at 1200 UTC 19 June, consistent with the time at which Chris was declared a tropical storm (Stewart 2013). Regarding thermostructural changes in the vertical, the CPS diagram reveals a straight transition from a deep cold core to a warm core of moderate vertical extent (Fig. 4b). Both thermal CPS metrics change their

signs during the second half of 18 June; $-V_T^U$ becomes positive 6 h later than $-V_T^L$ as the warm core extends in the vertical over time. On 20 June, Chris becomes affected by a second upper-level trough and thus acquires a slightly more asymmetric and shallower structure. Subsequent to this intermediate phase, Chris develops clear tropical characteristics in cyclone phase space, intensifies, and becomes a category 1 hurricane (Simpson 1974) at 0600 UTC 21 June (Stewart 2013).

4. Results

Consecutive ensemble forecasts initialized between 10 and 19 June are examined to address different aspects of predictability. Figure 5 shows how the number of similar tracks evolves as model initialization time gets closer to the tropical stage. The conspicuous increase in ensemble members predicting the pre-Chris cyclone on 15 June suggests the existence of a physical process limiting predictability. As will be shown below, the merging process between the upper-level cutoff low and

CHRIS (2012) [0.25° ECMWF Analysis]

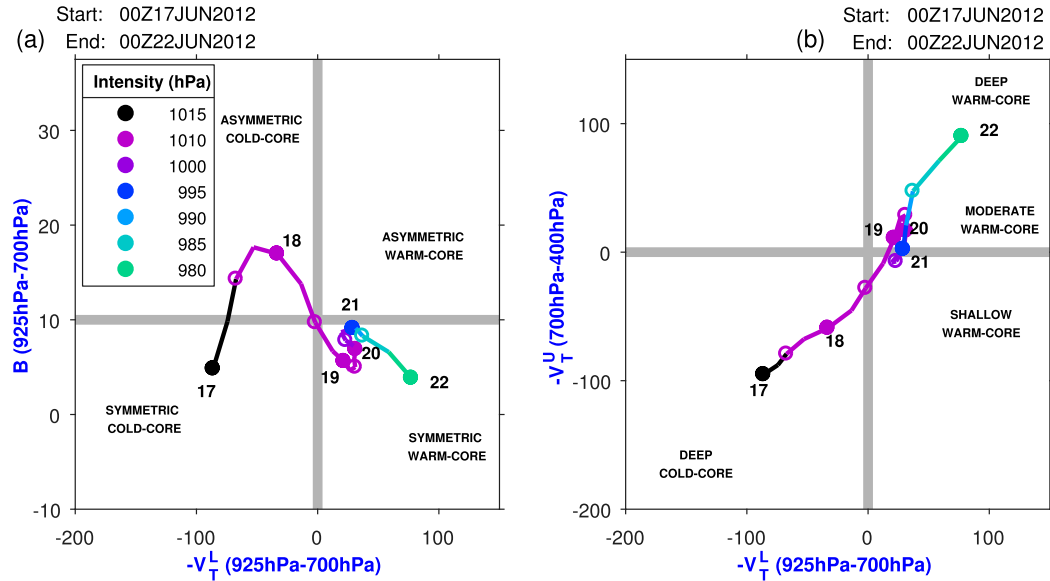


FIG. 4. Evolution of Hurricane Chris in the CPS. The calculated trajectory for the period from 0000 UTC 17 Jun to 0000 UTC 22 Jun 2012 is projected onto (a) the $B-V_T^L$ plane and (b) the $V_T^U-V_T^L$ plane. Two thick gray lines in each panel separate between four quadrants, representing different thermostructural cyclone stages (Hart 2003). Filled circles denote times at 0000 UTC and open circles denote times at 1200 UTC.

the PV remnants (features C and X in Fig. 2), as well as the representation of the overall structure of the resulting precursor trough (CX in Fig. 2) are major limitations at different lead times. Once the majority of the members predict a similar track, the main focus turns to the TT aspect to explore why some of the ensemble members acquire a more tropical structure, while the others remain less tropical. The section ends with a systematic investigation of predictability of Chris’s structural evolution.

a. Predictability of cyclone formation

Figure 6 displays normalized differences in 500–250-hPa layer-averaged PV of the combined ensemble forecasts from 0000 UTC 11 and 12 June between the *cyclone* ($\overline{d_{DTW}} \leq 700$ km) and *no-cyclone* ($\overline{d_{DTW}} > 700$ km) groups valid at two times on the merging day (15 June). Combining the two initialization times is reasonable, as both predict similar PV structures and areas of anomalies relative to the ensemble mean for the *cyclone* and *no-cyclone* groups. For forecasts initialized before 11 June, significant differences associated with the merging process are sparse and less coherent because of large spread in the ensemble. After the 12 June initialization, the two groups only exhibit minor differences as the initialization date gets closer to the merging day (not shown). This appears to be because all members share a similar depiction of the merging process at shorter lead times.

At the beginning of the merging day (15 June), the cutoff low (C), the trough (T), and the PV remnants (X) are in closer proximity in the *cyclone* group, whereas they are more separated in the *no-cyclone* group (Fig. 6a). In contrast to the isolated configuration in the *no-cyclone* composite, the cutoff low in the *cyclone*

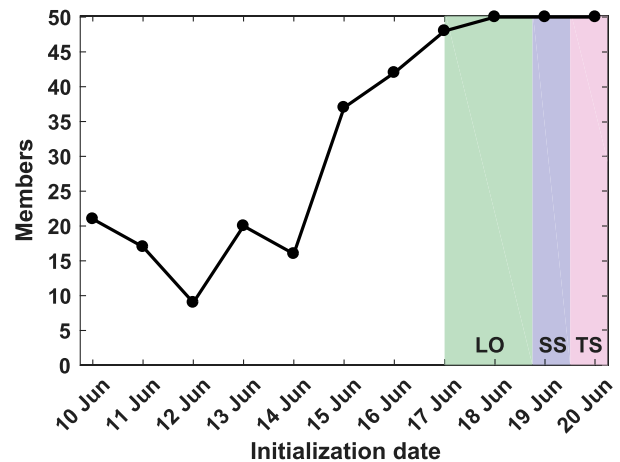


FIG. 5. Number of ECMWF ensemble members that feature a similar cyclone track for forecasts initialized at 0000 UTC between 10 Jun and 20 Jun 2012 (for more details on how similarity is measured see section 2c). The green, blue, and red areas highlight the periods when Chris was categorized as a “low,” “subtropical storm,” and “tropical storm,” respectively, by the National Hurricane Center.

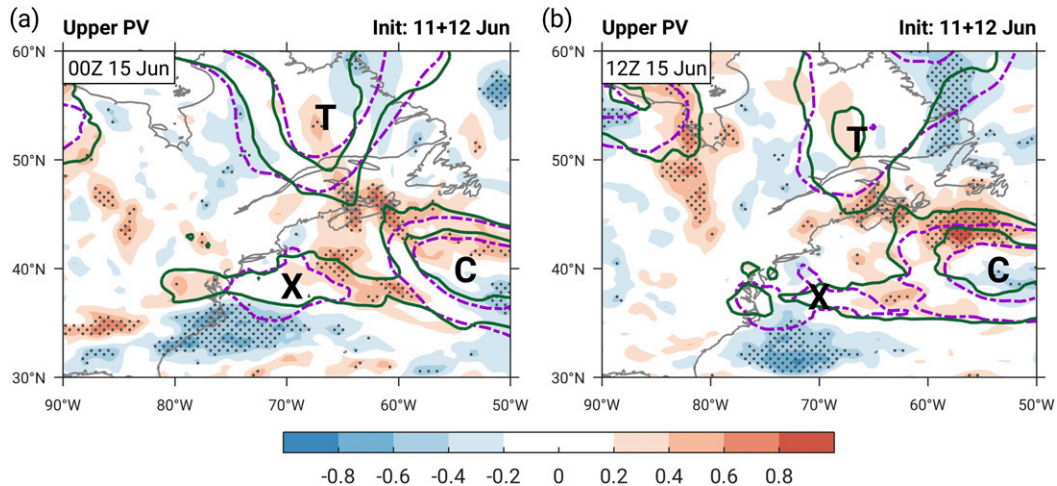


FIG. 6. Normalized difference in 500–250-hPa layer-averaged PV (shaded, units: standardized anomaly) between the *cyclone* and *no-cyclone* groups of the combined ensemble forecasts from 0000 UTC 11 and 12 Jun 2012 valid at (a) 0000 UTC 15 Jun and (b) 1200 UTC 15 Jun 2012. Differences significant at the 95% confidence level are indicated by gray stippling. The solid green *cyclone* group-averaged and dot-dashed purple *no-cyclone* group-averaged PV contours (at 1 and 2 PVU) serve as reference for the trough, cutoff low, and PV remnants, which are labeled with T, C, and X, respectively.

composite is more strongly interacting with the trough and has already merged with the PV remnants to the west, as can be seen from the 1 PVU (where $1 \text{ PVU} = 10^{-6} \text{ K kg}^{-1} \text{ m}^2 \text{ s}^{-1}$) contours and the significantly higher PV values between the three PV features. Concerning the strength and location of the interacting features, significantly enhanced PV along the northern gradient of the cutoff low reveals that the associated PV structure extends farther north in the *cyclone* group compared to the *no-cyclone* group. In addition, the *cyclone* group predicts higher PV values in the center of the trough encompassed by lower PV values to the east and west. This characterizes a narrower, but more intense trough, reaching slightly farther south.

Over the course of the merging day (15 June), the *cyclone* group shows the cutoff low (C) merged with the eastern part of the PV remnants (X); in contrast they are still separated in the *no-cyclone* group (Fig. 6b). The cutoff in the *cyclone* composite farther expands to the north relative to the *no-cyclone* composite and the trough (T) remains sharper. The pronounced PV maximum south of 55°N and the large significant negative area north of Newfoundland indicate a more negatively tilted trough compared to the *no-cyclone* group, favorable for a cyclonic PV roll-up (Shapiro et al. 1999).

Although the predictability of the merging process considerably improves after 12 June, a marked, concomitant rise in the number of similar tracks fails to materialize. Despite a slight increase between 12 and 13 June, the number of similar tracks still does not exceed the 21 members identified in the forecast from

10 June (Fig. 5). Only with the 15 June initialization, when the merging process was imminent, the ensemble statistics do show a prominent and rapid change from 16 to 37 members. To elucidate what caused this considerable doubling between 14 and 15 June, ensemble mean and standard deviation of the 500–250-hPa layer-averaged PV is shown for the time when the pre-Chris cyclone develops (0000 UTC 17 June) in Fig. 7. Comparing the shapes of the ensemble-averaged PV streamers, the forecasts from 14 June are broader and more positively tilted, with an elongated maximum in the middle of the filament (Fig. 7a). Predictions from the 15 June initialization more closely resemble the PV streamer identified in the analysis, with less implied westerly shear over the developing cyclone. A “notch” in the PV field northwest of the low center suggests that diabatic PV modification is already under way in many of the members by this time (cf. Fig. 7b and Fig. 3 of Davis and Bosart 2004). Regarding the western end of the PV streamer (west of 65°W), the ensemble forecast from 14 June is characterized by high standard deviations along its entire equatorward flank, whereas similar standard deviation values are found in a substantially smaller area between the PV maximum at the tip and the zonal part of the PV streamer in the forecast from 15 June (Fig. 7b). In this context, it is remarkable that the highest standard deviations are no longer collocated with the strongest PV gradients, but with the area where diabatic PV redistribution is expected. The spatial confinement of uncertainty to the center of rotation suggests that most of the ensemble members

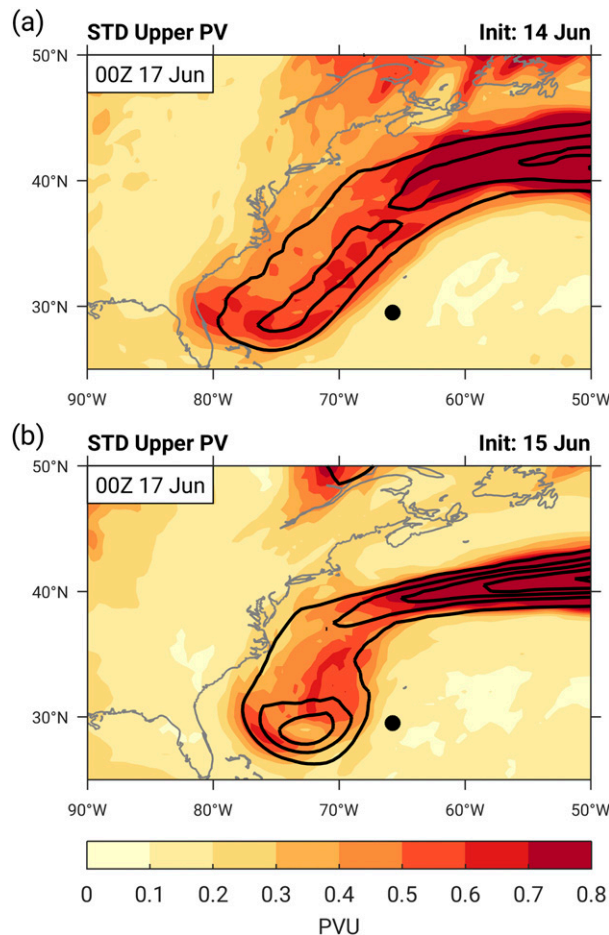


FIG. 7. Standard deviation of 500–250-hPa averaged PV (shaded, PVU) of the ensemble forecasts from (a) 0000 UTC 14 Jun and (b) 0000 UTC 15 Jun 2012, both valid at 0000 UTC 17 Jun 2012. The black ensemble-averaged PV contours (at 0.5-PVU intervals starting at 1 PVU) serve as reference and the black-filled circle marks the location of the pre-Chris cyclone in the analysis.

agree on the position and overall structure of the hook-shaped PV trough from the 15 June initialization onward. Examination of PV streamers among individual ensemble members corroborates this agreement (not shown). Thus, subsequent to the prediction of the PV merger, it is the prediction of the actual shape and position of the merged PV streamer that constitutes a dynamical factor limiting the predictability of the pre-Chris cyclone's formation, prior to the 15 June initialization.

The ensemble forecast initialized on 15 June is further explored in terms of differences between the upper-level PV streamers in the *cyclone* and *no-cyclone* groups to identify structural characteristics that promoted the development of Chris. Both groups exhibit the hook-shaped PV streamer with a distinct maximum at the southern tip (Fig. 8a), which suggests that the accurate

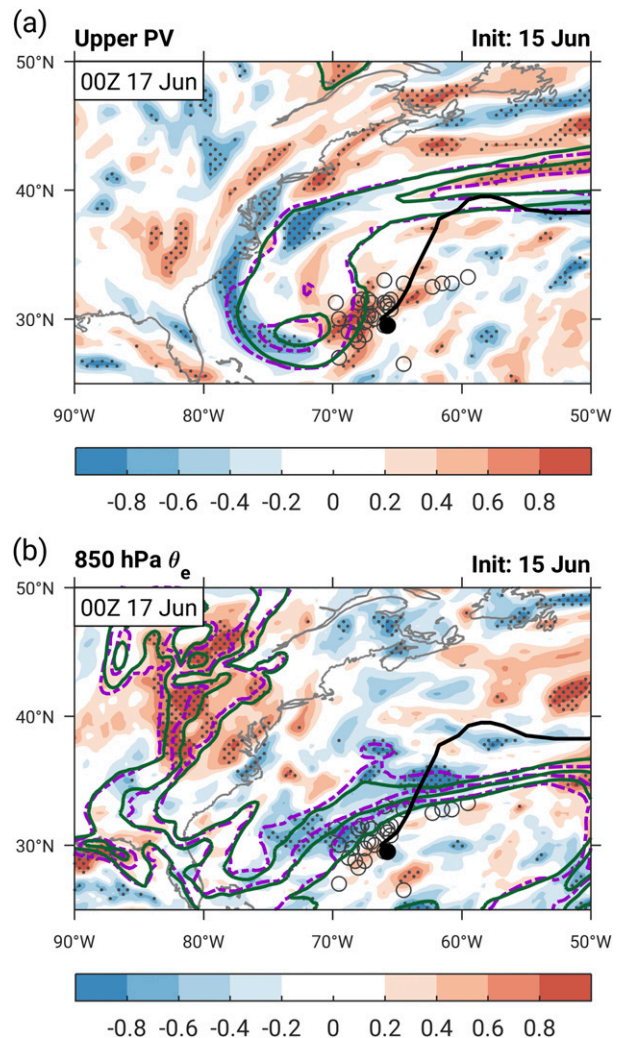


FIG. 8. (a) As in Fig. 6, but for the ensemble forecasts from 0000 UTC 15 Jun 2012 valid at 0000 UTC 17 Jun 2012. (b) As in (a), but for θ_e at 850 hPa (K) and with the solid green and dot-dashed purple θ_e contours (at 322, 326, and 330 K) indicating where the strongest gradients are located in the *cyclone* and *no-cyclone* groups, respectively. Open (filled) circles mark the cyclone locations in the *cyclone* group forecasts (analysis) at that time and the thick, black line shows the analysis track.

prediction of the PV streamer's shape is insufficient for forecasting the pre-Chris cyclone's formation. The intensity of the PV maximum is similarly forecasted among the two groups, but a zonal dipole in the group differences reveals that the PV trough is shifted farther east in the *cyclone* group, closer to the formation location of the pre-Chris cyclone. As indicated by the open circles, the majority of the developing cyclones (except for five members) is predicted to emerge between the pre-Chris cyclone's location in the analysis and the PV streamer, collocated with significantly higher PV values in the *cyclone* group.

CHRIS (2012) [0.25° ECMWF Ensemble]

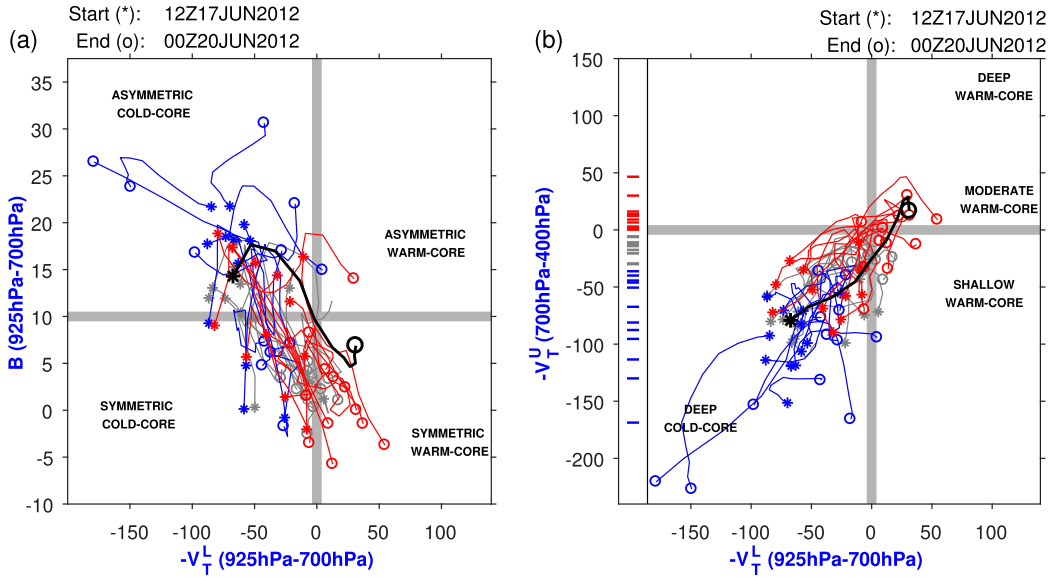


FIG. 9. As in Fig. 4, but for the *cyclone* group members in the ensemble forecast from 0000 UTC 15 Jun 2012 (colored) and for the analysis (black). Trajectories are shown from 1200 UTC 17 Jun to 0000 UTC 20 Jun 2012. The dashes in the left column of (b) show the distribution of the maximum $-V_T^U$ values reached between 0000 UTC 19 Jun and 0000 UTC 20 Jun 2012, separating the *warmer-core* (red), *intermediate-core* (gray), and *colder-core* (blue) terciles (see section 4b for more details); each trajectory is correspondingly colored. Stars and circles denote the start and end points of the tracks, respectively.

Examining the ensemble members from 15 June with regard to low-level thermodynamics, it becomes apparent that the location of the strongest θ_e gradient at 850 hPa is significantly different between the *cyclone* and *no-cyclone* groups (Fig. 8b). A broad area of significantly lower θ_e appears to the north and west of the developing cyclones, meaning that the location of the north-northwest to south-southeast θ_e gradient in the *no-cyclone* group is shifted, more distant from the formation locations in the *cyclone* group. The pattern suggests that there is enhanced baroclinicity underneath the eastern side of the upper-level PV streamer in the *cyclone* group compared to the *no-cyclone* group (investigation of corresponding θ plots confirms the comparison of baroclinicity). Therefore, it is the stronger lower-tropospheric θ_e gradients, equivalent to a more baroclinic environment, in superposition with the combination of the reduced vertical wind shear (cf. Figs. 7a,b), and the higher upper-tropospheric PV at the formation locations in the *cyclone* group that provide conditions more favorable for the formation of the pre-Chris cyclone.

b. Predictability of the TT of Chris

For all forecasts initialized after 14 June, the majority of the ensemble members features a similar track, and thus predicts the development of the pre-Chris cyclone

(Fig. 5). Therefore, the focus shifts to the predictability of the TT, and the 15 June initialization is investigated applying the partitioning strategy described in section 2d. Predicted cyclones in the 37 members of the *cyclone* group are split into three terciles (12 *warmer-core*, 13 *intermediate-core*, and 12 *colder-core* cyclones) based on the maximum $-V_T^U$ values reached between 0000 UTC 19 June and 0000 UTC 20 June. The results described here are qualitatively insensitive to changes in the size of the composite groups. The range of upper-level warm-core amplitudes is shown along the ordinate in Fig. 9b. Because the maxima of the *warmer-core* (*colder-core*) tercile are all positive (negative), these two groups of the 15 June initialization can be specified more precisely and are thus referred to as “*transition*” and “*no-transition*” groups hereafter. It is worth noting that the CPS-based partition method captures coherent cyclone-relative differences in cyclone structure for surface pressure, low-level wind speed, and θ_e (not shown).

A clear distinction in temporal evolution can be seen between the *transition* and *no-transition* groups in the CPS (Fig. 9). Compared to the analysis trajectory, most of the trajectories of the *no-transition* cyclones start as more intense cold cores while the *transition* cyclones have weaker cold cores on 17 June (Fig. 9b). Over the subsequent 2.5 days, the cores of the circulations in the *transition* group warm throughout the column. Those of

the *no-transition* category exhibit mixed behavior that ranges from the rapid warming of initially extreme cold-core circulations, to the deep cooling of more moderate initial structures. Concerning the cyclone symmetry (Fig. 9a), most of the trajectories of the *transition* group tend toward decreasing B , reaching values that represent a symmetric structure. In contrast, there is large variability in where the trajectories of the *no-transition* group end. About half of the cyclones attain a symmetric structure whereas the other half remains asymmetric.

1) ENVIRONMENTAL INFLUENCES

In the ensemble forecast initialized at 0000 UTC 15 June, different dynamical scenarios are found at 0000 UTC 18 June for the PV streamer associated with the *transition* and the *no-transition* groups, 1.5 days before the tropical stage in the analysis (Fig. 10). The *transition* group features a narrow, wrapping PV streamer, with predominantly higher PV appearing within the 1-PVU contour and significantly reduced PV in the middle of the hook (Fig. 10a). On the other hand, the PV trough in the *no-transition* group forms a broad, relatively incoherent structure, with significantly higher upper-level PV at its eastern flank. In contrast to the well-defined filament structure in the *transition* composite, the western part of the PV streamer has already degenerated. The *transition* cyclones predominantly evolve underneath or at the inner side of the narrow PV streamer, which is consistent with a composite study of 2004–08 North Atlantic TT cases (Galarneau et al. 2015). However, the *no-transition* cyclones tend to be located at the eastern edge of the broad PV trough, collocated with the area of relatively higher PV in this group. Another conspicuous difference between the groups is that the positions of the *transition* cyclones lie close together while those of the *no-transition* cyclones are spread along the leading edge of the streamer.

The predicted positions of the cyclones relative to the PV streamers determine to what extent they are exposed to the detrimental effect of vertical wind shear. Because the area within the roll-up of the PV streamer is associated with weaker 850–300-hPa wind shear ($5\text{--}20\text{ m s}^{-1}$), the *transition* cyclones occur in an environment that is more conducive to TT (Fig. 11a). The *no-transition* cyclones, however, experience higher shear along the eastern side of the broad upper-level PV structure, with magnitudes exceeding 20 m s^{-1} (Fig. 11b).

To examine thermodynamic distinctions in the ensemble forecast from 15 June, we focus on relative humidity because it complements the thermal differences already considered in the $-V_T^U$ -based separation by a moisture perspective. The most prominent aspect of Fig. 10b is again associated with the area within the

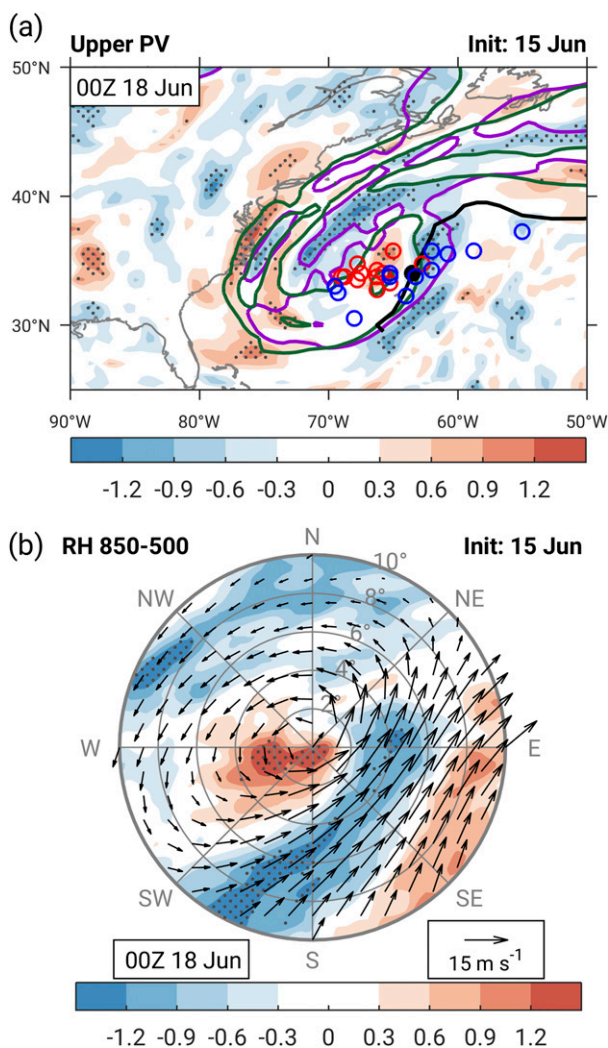


FIG. 10. (a) Normalized difference of 500–250-hPa layer-averaged PV (shaded, units: standardized anomaly) between the *transition* and *no-transition* groups of the ensemble forecasts from 0000 UTC 15 Jun 2012 valid at 0000 UTC 18 Jun 2012. The green *transition* and purple *no-transition* group-averaged PV contours (at 1 and 2 PVU) serve as reference. Red, blue, and black circles mark the cyclone locations in the *transition* group, *no-transition* group, and the analysis, respectively, at that time and the thick, black line shows the analysis track. (b) Normalized difference of cyclone-relative 850–500-hPa layer-averaged relative humidity (shaded, units: standardized anomaly) between the *transition* and *no-transition* groups of the ensemble forecasts from 0000 UTC 15 Jun 2012 valid at 0000 UTC 18 Jun 2012. Cyclone group-averaged wind vectors (m s^{-1}) are calculated for the same layer and scale with the reference vector in the bottom right. Differences significant at the 95% confidence level are indicated by gray stippling in (a) and (b).

wrapping PV streamer: the lower to middle troposphere is more moist for the *transition* compared to the *no-transition* composite. An isolated area of significantly higher relative humidity is found for the *transition* group just west of the center positions (Fig. 10b).

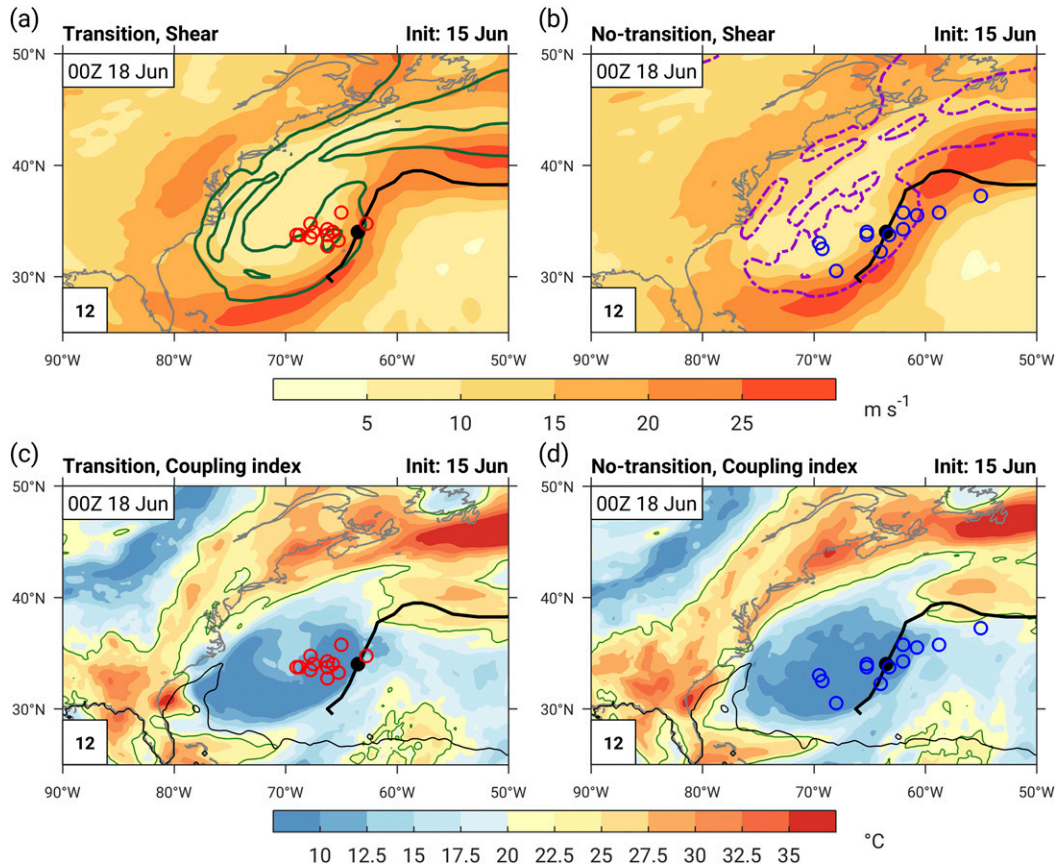


FIG. 11. Composite mean of (a),(b) 850–300-hPa shear magnitude (shaded, m s^{-1}) and (c),(d) coupling index (shaded, $^{\circ}\text{C}$) for (a),(c) the *transition* and (b),(d) the *no-transition* groups of the ensemble forecast from 0000 UTC 15 Jun 2012 valid at 0000 UTC 18 Jun 2012. In (a),(b), the solid green *transition* group-averaged and dot-dashed purple *no-transition* group-averaged PV contours (at 1 and 2 PVU) serve as reference. In (c),(d), black contours represent the canonical 26.5 $^{\circ}\text{C}$ threshold based on sea surface temperatures, whereas green contours highlight the 22.5 $^{\circ}\text{C}$ threshold for the coupling index. For the latter, lower values indicate favorable conditions for TC genesis via the TT pathway (McTaggart-Cowan et al. 2015). Red, blue, and black circles mark the cyclone locations in the *transition* group, *no-transition* group, and the analysis, respectively, at that time and the thick, black line shows the analysis track. The number at the bottom-left corner of each panel denotes the composite size.

The more pronounced hook shape of the PV trough in this group helps the moisture to be concentrated in this area. By contrast, the *no-transition* cyclones are surrounded by a drier environment in the middle of the broad PV structure and more moist conditions along the eastern flank of the PV streamer. Thus, as noted for the TT of Chris in the analysis, the cyclonic roll-up of the PV streamer in the *transition* group causes the seclusion of a warm and moist air mass, leading to deep warming of the core in an environment conducive to TT (cf. Figs. 3d,f). Less moist conditions result from the predicted PV dynamics in the *no-transition* group, so the cyclones fail to transition to a TC. Inspection of the composites up to 12 h before and after 0000 UTC 18 June confirms that all (thermo)dynamic patterns of group differences remain qualitatively unchanged over this period.

Although the group composites show marked thermodynamic differences in the local environment, the coupling index (Bosart and Lackmann 1995) shows much smaller differences in large-scale stability. The coupling index is calculated as the difference between potential temperature θ on the dynamic tropopause at 2 PVU and θ_e at 850 hPa, and thus links the upper and lower levels, assessing the convective stability in the free atmosphere (McTaggart-Cowan et al. 2015). In both subsets, the cyclones are located in areas where the coupling index drops to values of less than 10 $^{\circ}\text{C}$ (Figs. 11c,d). This is well below the 22.5 $^{\circ}\text{C}$ maximum threshold proposed by McTaggart-Cowan et al. (2015) as an alternative to the canonical 26.5 $^{\circ}\text{C}$ -SST-based threshold for TC genesis (Gray 1968). From a (thermo)dynamic perspective, the crucial point in terms of the predictability

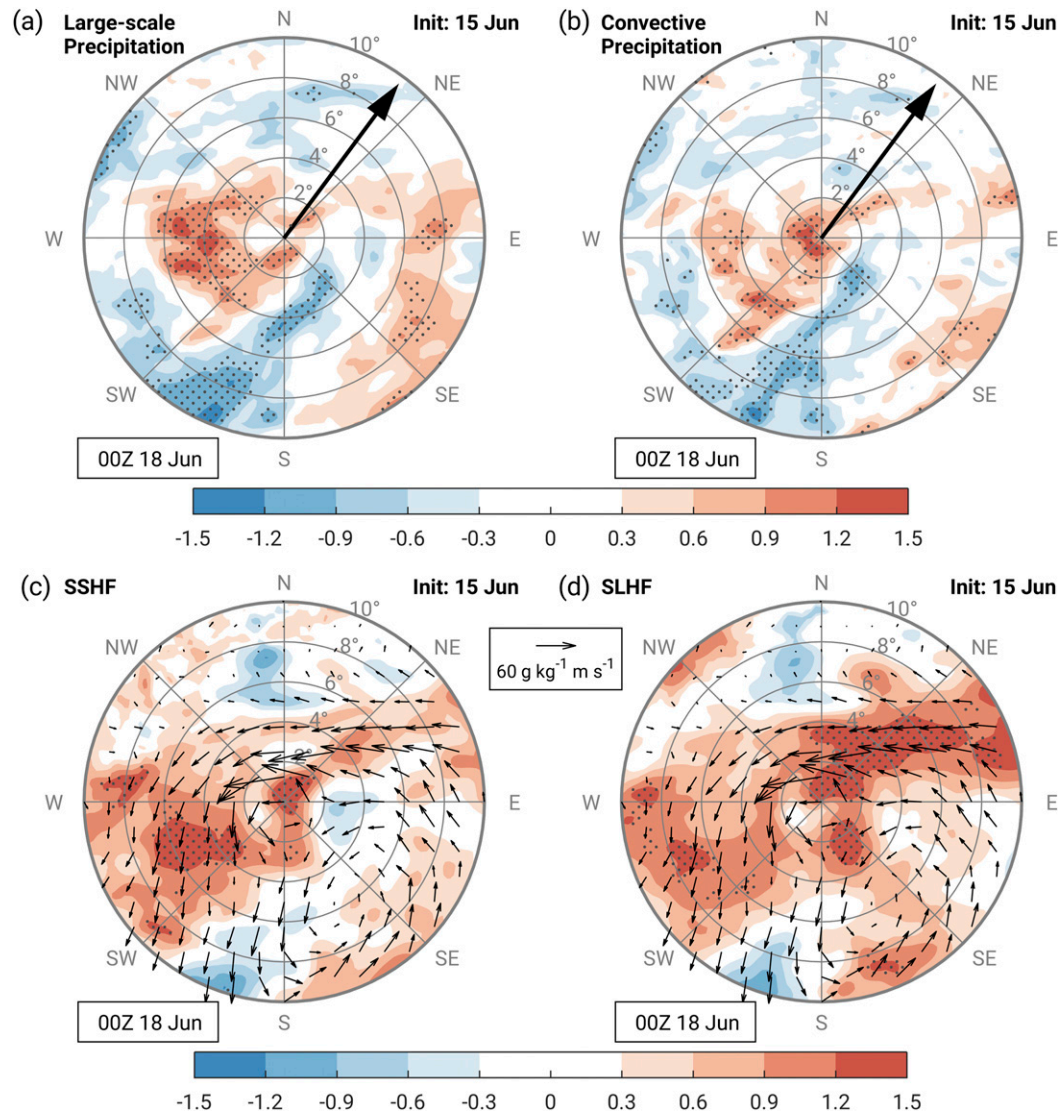


FIG. 12. As in Fig. 10b, but for (a) large-scale precipitation rate (mm h^{-1}), (b) convective precipitation rate (mm h^{-1}), (c) surface sensible heat fluxes (W m^{-2}), and (d) surface latent heat fluxes (W m^{-2}). Differences significant at the 95% confidence level are indicated by gray stippling. Cyclone group-averaged shear vectors are represented by thick black arrows in (a) and (b). In (c),(d), vectors show group differences for 925–850-hPa layer-averaged moisture flux ($\text{g kg}^{-1} \text{m s}^{-1}$), which scale with the reference vector in the middle.

of Chris' TT at 4.5 days of lead time is therefore not whether the forecasts predict climatologically favorable conditions in terms of convective stability, but rather how the warm and moist air mass is deformed by the PV merger and resulting streamer roll-up process.

2) CONVECTIVE ORGANIZATION

The distinctly predicted thermodynamic environments, in which the *transition* and *no-transition* cyclones develop, provide different conditions for the organization of moist convection that is necessary for a successful TT

(Davis and Bosart 2004). Even though the ECMWF model considered in this study deploys parameterization schemes for convection and boundary layer processes, and absolute values of parameterization-based variables are thus less reliable, differences between the partitioned groups still should be consistent with the thermodynamic scenarios described previously.

In Figs. 12a and 12b, composites of cyclone-relative differences in precipitation rates for the forecast initialized on 15 June are presented as a proxy for differences in moist convection, and thus approximately in vertical motion. This is reasonable since differences in

moisture availability between the *transition* and *no-transition* groups are negligible (not shown). As the large-scale precipitation rate suggests, the two distinct PV structures in the upper-troposphere are associated with significant differences in large-scale lifting (Fig. 12a). The warm and moist area enclosed by the PV streamer (cf. Fig. 10b) features significantly higher large-scale precipitation rates, which is equivalent to stronger upward motions, in the *transition* composite, compared to the *no-transition* group (cf. Fig. 10b). The overall pattern of differences in the convective precipitation is similarly predicted, however, with stronger signals within a radius of 2° (Fig. 12b). A comparison of the absolute precipitation rates of both variables reveals that the convectively generated vertical motion dominates over the large-scale ascent (not shown). Because of the upshear position of the stronger convection in the *transition* group, the divergent outflow aloft results in a more substantial reshaping of the upper-level PV trough (Davis and Bosart 2003, 2004). As a consequence of this, vertical wind shear is reduced to a greater extent, providing a cyclone environment more favorable for TT.

The combination of surface heat fluxes and low-level moisture flux vectors in Figs. 12c and 12d suggests that the warm and moist air mass in the midtroposphere builds from below and becomes secluded by the PV streamer in the *transition* group. The large area of stronger precipitation, and thus enhanced upward motion, west of the *transition* cyclone centers (Figs. 12a,b) appears to be in high spatial congruence with significantly increased surface sensible heat fluxes from the ocean into the atmosphere (Fig. 12c). By contrast, the most striking feature for differences in surface latent heat fluxes is linked to the warm seclusion in the *transition* group. A narrow band of significantly higher surface latent heat fluxes to the northeast occurs in the same area where easterly low-level moisture flux vector differences indicate stronger westward moisture transport by the alongfront flow. This resembles the feature found to be associated with transitioning cyclones in a multicase study from Galarneau et al. (2015, cf. their Figs. 3d,e). It can be thus assumed that the enhanced surface latent heat fluxes provide the moisture, which then gets transported along the frontal zone into the region of enhanced upward motions, where it partly converges, eventually increasing midtropospheric θ_e through large-scale lifting and convective transport. It is apparently the lack of surface latent heat fluxes and subsequent moisture transport that primarily prevented the *no-transition* cyclones from acquiring organized and sustained convection for an amplification and transition into a TC.

c. Predictability of structural evolution

Following the previous examinations of individual verification times for the ensemble forecast initialized at 0000 UTC 15 June, a systematic investigation of the ensemble forecasts initialized between 10 and 19 June with respect to the CPS metrics, as well as environmental and structural cyclone properties provide a more general perspective on the predictability of Chris's tropical characteristics. As described in section 2d, the CPS trajectories for each ensemble forecast are separated into *warmer-core*, *intermediate-core*, and *colder-core* terciles based on the maximum $-V_T^U$ values reached between 0000 UTC 19 June and 0000 UTC 20 June. Using these group memberships, the maximum $-V_T^U$ and minimum B values are also determined within the 24-h period. The main features of the obtained statistics are visualized in Fig. 13. Chris's upper-level warm core is greatly underestimated by all members before the initialization on 13 June, while almost every identified cyclone undergoes TT from 18 June onward (Fig. 13a). The distinction between *warmer-core* and *colder-core* cyclones is thus particularly reasonable for the medium-range ensemble forecasts initialized between 13 and 17 June (yellow frame) and so the following discussion will focus on this period.

Because the $-V_T^U$ and $-V_T^L$ metrics are closely related in this case, the *warmer-core* terciles predominately exhibit warm cores and the *colder-core* terciles exhibit cold cores in the lower troposphere (Fig. 13b). The *warmer-core* cyclones also tend to be more symmetric than the *colder-core* cyclones throughout the ensemble forecasts from 13 to 17 June (Fig. 13c). A marked reduction in both the differences between the *warmer-core* and *colder-core* structures, and the range of structures within each group, occurs between 15 and 16 June (lead time of 3.5–4.5 days). This abrupt change in predictability is most noticeable for $-V_T^U$ and B (Fig. 13a,c). These prominent changes in the forecast spread are due to the remaining uncertainty that is associated with the prediction of the warm and moist seclusion that limits predictability in the 15 June initialization (not shown).

Applying the $-V_T^U$ -based group memberships to the environmental shear and to properties indicative of cyclone structure and intensity, results demonstrate that the *warmer-core* cyclones can be distinguished from the *colder-core* cyclones in the ensemble forecasts initialized up to one week before the tropical stage (Fig. 14). In terms of the 850–200-hPa environmental shear calculated over a 200–800-km annulus, the majority of the *warmer-core* cyclones experience favorable conditions as shear drops to values generally less than 10 m s^{-1} (Fig. 14a). For the 17 June initialization, the upper-level

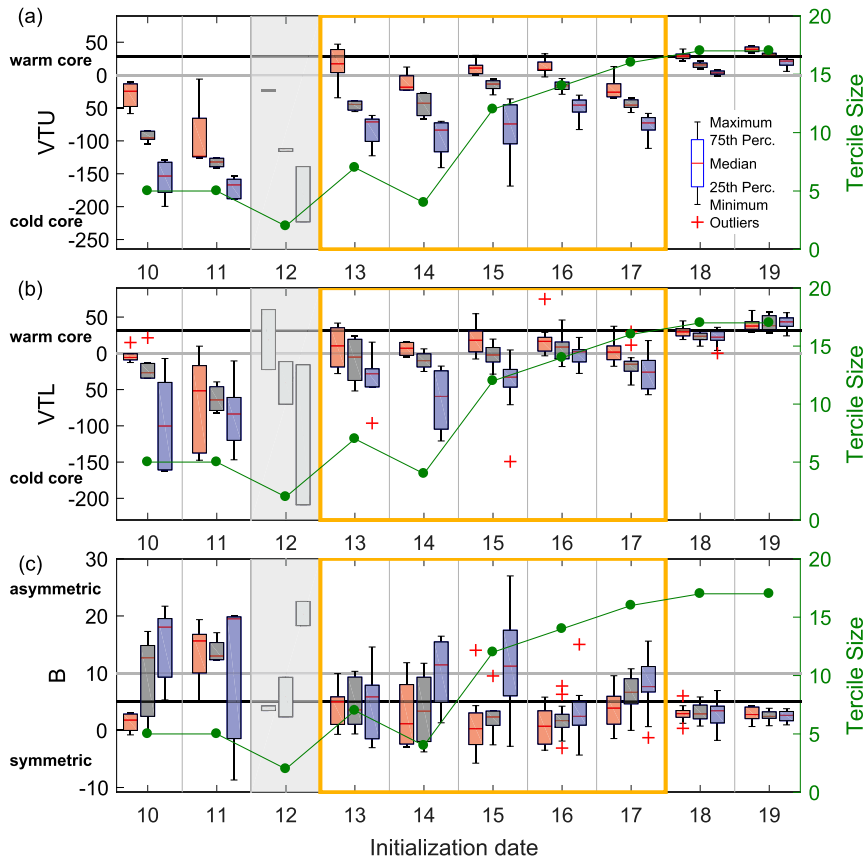


FIG. 13. Statistical overview of how the ensemble forecasts from 10 to 19 Jun 2012 predict (a) the maximum $-V_T^U$, (b) the maximum $-V_T^L$, and (c) the minimum B metric reached between 0000 UTC 19 Jun and 0000 UTC 20 Jun. Similar to the approach in Fig. 9, ensemble members are separated into warm (red), intermediate (gray), and cold (blue) terciles based on the $-V_T^U$ metric. Since the terciles from 12 Jun only consist of two members, the results of this ensemble forecast lack robustness and are hence disregarded (light gray shading). For each category, a box-and-whisker plot displays the median (red line), the interquartile range (IQR, box length), the most extreme values not considered as outliers (whiskers, maximum 1.5 times the IQR), and the outliers (red crosses). Horizontal black lines indicate the analysis values at 1200 UTC 19 Jun, and the green lines show how tercile sizes change with lead time. Yellow boxes indicate the most relevant initialization dates.

PV streamers above the low-level cyclones are predicted to be broader and more intense compared to the 16 June initialization, leading to an increase in shear for all three groups, consistent with decreased estimates of warm-core strength (Figs. 13a,b). The *colder-core* group consistently predicts a much larger range of shear, in particular for 14 and 15 June, with detrimental shear magnitudes of $15\text{--}20\text{ m s}^{-1}$. Because strong shear imposed on a TC increases baroclinicity, and thus the cyclone's thickness asymmetry, these changes in the forecast uncertainty are consistent with the ones described by the B metric (see Fig. 13c). Using the minimum MSLP for intensity, the *warmer-core* cyclones are readily distinguished from the *colder-core* cyclones because the former acquire significantly

lower minima in most of the ensemble forecasts (Fig. 14b). Only minor differences are apparent in the ensemble statistics for lower-level wind speed between the *warmer-core* and *colder-core* groups (not shown). Instead, the radius of maximum wind describes the compactness of the forecasted cyclones (Fig. 14c). Despite the fact that the *warmer-core* cyclones from 14 and 17 June have neutral or weak warm cores (Figs. 13a,b), their wind fields are more compact than those of the *colder-core* group, further suggesting that the *warmer-core* cyclones exhibit a more tropical structure. Similar to the CPS metrics, the spread of the ensemble forecasts collapses markedly after the upper-level PV features merged by early 16 June.

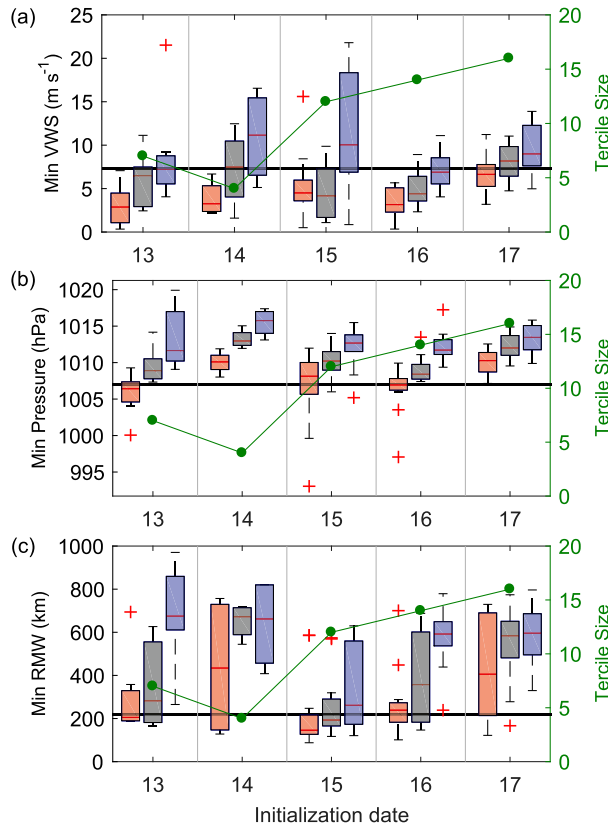


FIG. 14. As in Fig. 13, but for (a) minimum 850–200-hPa vertical wind shear (m s^{-1}) averaged between the radius of 200 and 800 km, (b) minimum central pressure (hPa), and minimum radius of maximum wind (km) for ensemble forecasts initialized between 13 and 17 Jun 2012.

5. Discussion and conclusions

The aim of the current case study is to systematically investigate a TT event and to identify major limitations for predictability of (i) the formation of the pre-tropical cyclone, (ii) its TT, and (iii) the structural evolution from an ensemble perspective. For this purpose, North Atlantic Hurricane Chris (2012) was chosen because of the complex antecedent PV dynamics and the strong baroclinic environment in the upper and lower levels that facilitated the development of the extratropical precursor cyclone. Before the TC emerged, the predictability at different baroclinic stages is limited by a sequence of events: (i) anticyclonic Rossby-wave breaking, (ii) the merger of vortex-like PV features, and (iii) the cyclonic roll-up of the resultant PV streamer. Ranging from synoptic-scale PV dynamics to differences in the convective organization, this study seeks to provide a better understanding of potential sources of uncertainty that are associated with these atmospheric features and processes across a broad range of scales.

The results of this investigation show that the predictability of the pre-Chris cyclone's formation is strongly related to the predictability of the preceding PV dynamics. At 5–6-day lead times (11 and 12 June) prior to the development of the pre-Chris cyclone, formation of the pre-Chris cyclone was only predicted by ensemble members that successfully merged pre-existing PV remnants and a cutoff low to develop the precursor PV trough. Once the majority of the members predicted the PV merger 4 days before the pre-Chris cyclone formation (13–15 June initializations in Fig. 15c), the number of similar cyclone tracks rises (Fig. 15d). This conspicuous increase in predictability appears to be related to the fact that the anticyclonic wave break has already generated the critical upper-level cutoff low by this time (Fig. 15a), and uncertainty associated with the existence of the cutoff low is therefore dramatically reduced. The largest increase in the predictability of cyclone formation, however, takes place between 3 and 2 days prior to the formation of the pre-Chris cyclone (14–15 June), when the bulk uncertainty in the area of the PV trough becomes restricted to the interior of the cyclonic PV streamer roll-up. This regime change in predictability is found to be attributable to the PV merging that was imminent on that day (cf. Figs. 15a,c,d). A more detailed analysis of the resultant trough structures reveals that the members predicting the formation of the pre-Chris cyclone are linked to a superposition of higher PV values at upper levels and stronger thermal gradients at lower levels (i.e., an overall stronger baroclinic environment). These findings corroborate the conjecture of Wang et al. (2018) that the set of factors relevant for tropical cyclogenesis [e.g., absolute vorticity, relative humidity, potential intensity, and vertical wind shear in the genesis potential index of Emanuel and Nolan (2004)] needs to be extended for the TT pathways. Because these factors generally represent tropical ingredients and thus predominantly nonbaroclinic conditions, further research is required to determine how the baroclinic precursor dynamics involved in the TT pathways could be incorporated into a conceptual or practical model of TT likelihood.

Because this case study aims to document the predictability of TT, further examination is performed to elucidate why some of the forecasted developing cyclones in the ensemble successfully complete TT. Simulations begin to accurately predict TT almost 1 week before TT occurs, at the time when most ensemble members agree on the PV merger (cf. Figs. 15c,d). The increased predictability of the PV merger, and hence the formation of the upper-level precursor PV trough, appears to lead to these first TT predictions. It is somewhat surprising that no considerable increase in the proportion of the

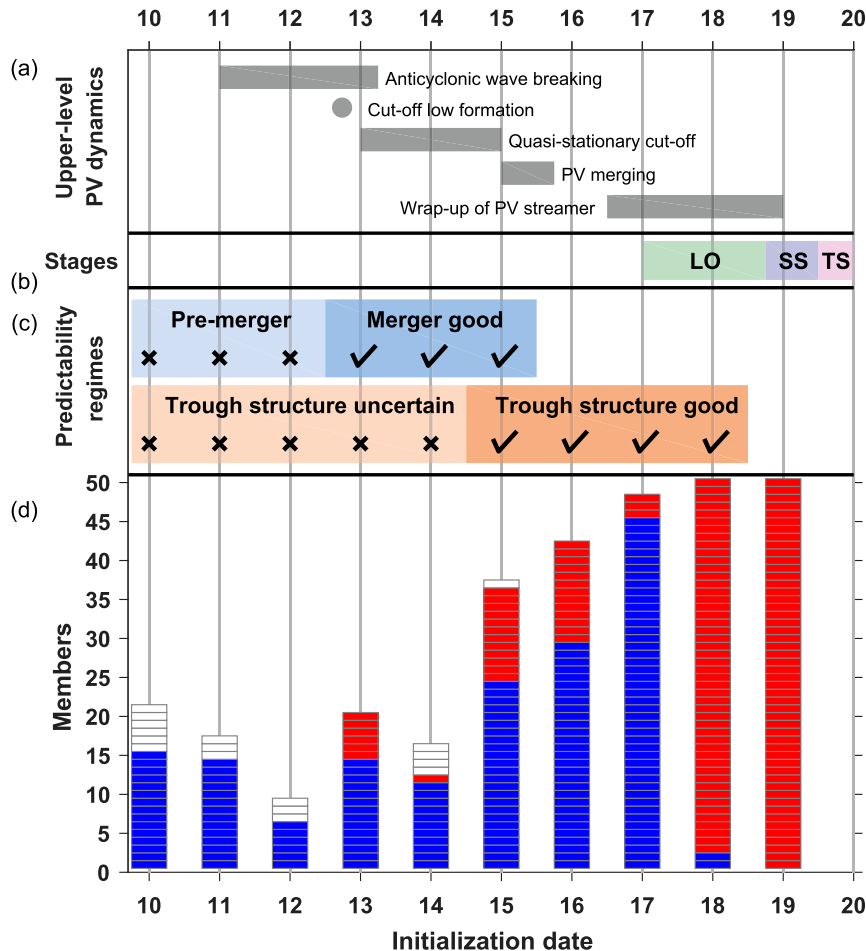


FIG. 15. Schematic diagram summarizing the predictability of Hurricane Chris between 10 and 19 Jun 2012: (a) crucial periods (bars) and events (points) in the upper-level PV dynamics of the analysis (cf. section 3), (b) stages in the NHC best track, and (c) identified predictability regimes with an assessment of whether the atmospheric process or feature is not (crosses) or is “sufficiently” well (ticks) predicted in the ensemble forecasts. (d) Overview of the ensemble predictive skill, with the height of the stacked bars indicating the number of identified similar tracks and the red (warm core), and blue (cold core) segment colors corresponding to the maximum $-V_T^U$ value reached between 0000 UTC 19 Jun and 0000 UTC 20 Jun 2012. Un-colored segments indicate that the similar cyclone track ends before 0000 UTC 19 Jun.

warm-core cyclones is found in the subsequent initializations, until the cyclone itself has developed (at some lead times, even fewer TTs occur). The majority of ensemble members predict a warm core only after the pre-Chris cyclone became located underneath the PV streamer 1.5 days before the tropical phase. This study confirms the findings of Majumdar and Torn (2014), who also identify low predictive skill in ECMWF short-range ensemble predictions of 2010–12 North Atlantic warm-core formations for lead times longer than 1–2 days.

Composite differences between the warmest and coldest upper-level cores in the forecast initialization from 0000 UTC 15 June are analyzed during the roll-up of the PV streamer to highlight the (thermo)dynamics

that assist or impede the cyclone’s completion of TT. From a dynamical perspective, the shape of the PV streamer in combination with the relative cyclone position are most decisive in determining whether TT occurs. Similar to the findings of Galarneau et al. (2015), the *transition* cyclones are located inside a narrow, wrapping PV streamer and interact with the high-PV feature at a shorter distance compared to the *no-transition* cyclones. The latter are steered northeastward along the leading edge of a broad but incoherent PV structure. Reduced vertical shear characterizes the near-cyclone environment in the *transition* cases. The distinct upper-level PV dynamics are also related to different thermodynamic scenarios. The narrow PV streamer in

the *transition* cases lead to the isolation of a warm, moist air mass primarily in the midtroposphere, which provides a more tropical environment. Conversely, detrimental dry air ahead of the PV trough is found in the members whose predicted cyclones fail to complete TT.

In terms of convective organization, enhanced surface latent heat fluxes northeast of the *transition* centers increase the low-level moisture take-up, which in turn increases the alongfront moisture fluxes into a convergent region associated with strong upward motion, confirming the multicase study results from Galarneau et al. (2015). In accordance with the conceptual model from Davis and Bosart (2004, their Fig. 3), the upstream position of the enhanced convection leads to a stronger reduction in vertical wind shear.

The present study has also shown that it is possible to make a skillful distinction between *warmer-core* and *colder-core* cyclones in CPS metrics, and environmental and structural cyclone properties in medium-range forecasts. In agreement with the findings of Davis and Bosart (2003), deep-layer wind shear below 10 m s^{-1} appears to be favorable for TT. With regard to the CPS metrics, substantial forecast improvements are linked to the end of the upper-level PV merger as well as to the time when the upper-tropospheric PV trough connects to the nontropical precursor cyclone. This suggests that interactions of baroclinic features prior to TT are major sources of forecast uncertainties for this TC development pathway.

The present study is the first to investigate changes in predictability of a TT event with lead time in order to identify the major limiting factors in the antecedent dynamics. Various atmospheric features and processes are found to significantly affect predictability. The consistency of these features with previous climatological investigations suggests that the associated predictability limitations may be also relevant for other TT cases. Further research is required to identify other relevant features and to understand better their relative importance to predictability, ideally using a feature-based framework. The results of such an investigation will be reported in a future study that will further quantify the predictability of TC formation via the TT pathway. Moreover, the methods developed here open a promising avenue to multiscale predictability studies of TTs in all basins.

Acknowledgments. The research leading to these results has been accomplished within project C3 “Multi-scale dynamics and predictability of Atlantic Subtropical Cyclones and Medicanes” of the Transregional Collaborative Research Center SFB/TRR 165 “Waves to Weather” funded by the German Science Foundation (DFG). We thank the

editor, two anonymous reviewers, and Alex Kowaleski for their critical and constructive comments that helped to improve significantly the quality of the paper. The authors also thank Andreas Schlueter and various other colleagues for helpful discussions.

REFERENCES

- Bentley, A. M., D. Keyser, and L. F. Bosart, 2016: A dynamically based climatology of subtropical cyclones that undergo tropical transition in the North Atlantic basin. *Mon. Wea. Rev.*, **144**, 2049–2068, <https://doi.org/10.1175/MWR-D-15-0251.1>.
- , L. F. Bosart, and D. Keyser, 2017: Upper-tropospheric precursors to the formation of subtropical cyclones that undergo tropical transition in the North Atlantic basin. *Mon. Wea. Rev.*, **145**, 503–520, <https://doi.org/10.1175/MWR-D-16-0263.1>.
- Berndt, D. J., and J. Clifford, 1994: Using dynamic time warping to find patterns in time series. *Proc. AAAI Workshop on Knowledge Discovery in Databases*, Seattle, WA, AAAI Press, Vol. 10, AAAI Tech. Rep. WS-94-03, 359–370, <http://www.aaai.org/Papers/Workshops/1994/WS-94-03/WS94-03-031.pdf>.
- Bosart, L. F., and G. M. Lackmann, 1995: Postlandfall tropical cyclone reintensification in a weakly baroclinic environment: A case study of Hurricane David (September 1979). *Mon. Wea. Rev.*, **123**, 3268–3291, [https://doi.org/10.1175/1520-0493\(1995\)123<3268:PTCRIA>2.0.CO;2](https://doi.org/10.1175/1520-0493(1995)123<3268:PTCRIA>2.0.CO;2).
- Chen, L., and R. Ng, 2004: On the marriage of Lp-norms and edit distance. *Proc. 30th Int. Conference on Very Large Data Bases*, Vol. 30, Toronto, Ontario, Canada, VLDB, 792–803.
- Davis, C. A., and L. F. Bosart, 2003: Baroclinically induced tropical cyclogenesis. *Mon. Wea. Rev.*, **131**, 2730–2747, [https://doi.org/10.1175/1520-0493\(2003\)131<2730:BITC>2.0.CO;2](https://doi.org/10.1175/1520-0493(2003)131<2730:BITC>2.0.CO;2).
- , and —, 2004: The TT problem: Forecasting the tropical transition of cyclones. *Bull. Amer. Meteor. Soc.*, **85**, 1657–1662, <https://doi.org/10.1175/BAMS-85-11-1657>.
- Elsner, J. B., G. S. Lehmiller, and T. B. Kimberlain, 1996: Objective classification of Atlantic hurricanes. *J. Climate*, **9**, 2880–2889, [https://doi.org/10.1175/1520-0442\(1996\)009<2880:OCOAH>2.0.CO;2](https://doi.org/10.1175/1520-0442(1996)009<2880:OCOAH>2.0.CO;2).
- Emanuel, K. A., and D. S. Nolan, 2004: Tropical cyclone activity and the global climate system. *26th Conf. on Hurricanes and Tropical Meteorology*, Miami, FL, Amer. Meteor. Soc., 10A.2, https://ams.confex.com/ams/26HURR/techprogram/paper_75463.htm.
- Evans, J. L., and M. P. Guishard, 2009: Atlantic subtropical storms. *Mon. Wea. Rev.*, **137**, 2065–2080, <https://doi.org/10.1175/2009MWR2468.1>.
- Galarneau, T. J., Jr., R. McTaggart-Cowan, L. F. Bosart, and C. A. Davis, 2015: Development of North Atlantic tropical disturbances near upper-level potential vorticity streamers. *J. Atmos. Sci.*, **72**, 572–597, <https://doi.org/10.1175/JAS-D-14-0106.1>.
- González-Alemán, J. J., F. Valero, F. Martín-León, and J. L. Evans, 2015: Classification and synoptic analysis of subtropical cyclones within the northeastern Atlantic Ocean. *J. Climate*, **28**, 3331–3352, <https://doi.org/10.1175/JCLI-D-14-00276.1>.
- , J. L. Evans, and A. Kowaleski, 2018: Use of ensemble forecasts to investigate synoptic influences on the structural evolution and predictability of Hurricane Alex (2016) in the midlatitudes. *Mon. Wea. Rev.*, **146**, 3143–3162, <https://doi.org/10.1175/MWR-D-18-0015.1>.
- Gray, W. M., 1968: Global view of the origin of tropical disturbances and storms. *Mon. Wea. Rev.*, **96**, 669–700, [https://doi.org/10.1175/1520-0493\(1968\)096<0669:GVOTOO>2.0.CO;2](https://doi.org/10.1175/1520-0493(1968)096<0669:GVOTOO>2.0.CO;2).

- Hart, R. E., 2003: A cyclone phase space derived from thermal wind and thermal asymmetry. *Mon. Wea. Rev.*, **131**, 585–616, [https://doi.org/10.1175/1520-0493\(2003\)131<0585:ACPSDF>2.0.CO;2](https://doi.org/10.1175/1520-0493(2003)131<0585:ACPSDF>2.0.CO;2).
- Hess, J. C., J. B. Elsner, and N. E. LaSeur, 1995: Improving seasonal hurricane predictions for the Atlantic basin. *Wea. Forecasting*, **10**, 425–432, [https://doi.org/10.1175/1520-0434\(1995\)010<0425:ISHPFT>2.0.CO;2](https://doi.org/10.1175/1520-0434(1995)010<0425:ISHPFT>2.0.CO;2).
- Hulme, A. L., and J. E. Martin, 2009: Synoptic- and frontal-scale influences on tropical transition events in the Atlantic basin. Part I: A six-case survey. *Mon. Wea. Rev.*, **137**, 3605–3625, <https://doi.org/10.1175/2009MWR2802.1>.
- Majumdar, S. J., and R. D. Torn, 2014: Probabilistic verification of global and mesoscale ensemble forecasts of tropical cyclogenesis. *Wea. Forecasting*, **29**, 1181–1198, <https://doi.org/10.1175/WAF-D-14-00028.1>.
- McTaggart-Cowan, R., G. D. Deane, L. F. Bosart, C. A. Davis, and T. J. Galarneau Jr., 2008: Climatology of tropical cyclogenesis in the North Atlantic (1948–2004). *Mon. Wea. Rev.*, **136**, 1284–1304, <https://doi.org/10.1175/2007MWR2245.1>.
- , T. J. Galarneau Jr., L. F. Bosart, R. W. Moore, and O. Martius, 2013: A global climatology of baroclinically influenced tropical cyclogenesis. *Mon. Wea. Rev.*, **141**, 1963–1989, <https://doi.org/10.1175/MWR-D-12-00186.1>.
- , E. L. Davies, J. G. Fairman Jr., T. J. Galarneau Jr., and D. M. Schultz, 2015: Revisiting the 26.5°C sea surface temperature threshold for tropical cyclone development. *Bull. Amer. Meteor. Soc.*, **96**, 1929–1943, <https://doi.org/10.1175/BAMS-D-13-00254.1>.
- Neu, U., and Coauthors, 2013: IMILAST: A community effort to intercompare extratropical cyclone detection and tracking algorithms. *Bull. Amer. Meteor. Soc.*, **94**, 529–547, <https://doi.org/10.1175/BAMS-D-11-00154.1>.
- Picornell, M. A., J. Campins, and A. Jansà, 2014: Detection and thermal description of medicanes from numerical simulation. *Nat. Hazards Earth Syst. Sci.*, **14**, 1059–1070, <https://doi.org/10.5194/nhess-14-1059-2014>.
- Postel, G. A., and M. H. Hitchman, 1999: A climatology of Rossby wave breaking along the subtropical tropopause. *J. Atmos. Sci.*, **56**, 359–373, [https://doi.org/10.1175/1520-0469\(1999\)056<0359:ACORWB>2.0.CO;2](https://doi.org/10.1175/1520-0469(1999)056<0359:ACORWB>2.0.CO;2).
- Sakoe, H., and S. Chiba, 1978: Dynamic programming algorithm optimization for spoken word recognition. *IEEE Trans. Acoust. Speech Signal Process.*, **26**, 43–49, <https://doi.org/10.1109/TASSP.1978.1163055>.
- Shapiro, M., and D. Keyser, 1990: Fronts, jet streams, and the tropopause. *Extratropical Cyclones: The Erik Palmén Memorial Volume*, C. W. Newton and E. Holopainen, Eds., Amer. Meteor. Soc., 167–191.
- , and Coauthors, 1999: A planetary-scale to mesoscale perspective of the life cycles of extratropical cyclones: The bridge between theory and observations. *The Life Cycles of Extratropical Cyclones*, M. A. Shapiro and S. Gronas, Eds., Amer. Meteor. Soc., 139–185.
- Simpson, R. H., 1974: The hurricane disaster-potential scale. *Weatherwise*, **27**, 169, <https://doi.org/10.1080/00431672.1974.9931702>.
- Stewart, S. R., 2013: Tropical Cyclone Report Hurricane Chris (18–22 June 2012). NHC Rep. AL032012, National Hurricane Center, 16 pp., https://www.nhc.noaa.gov/data/tcr/AL032012_Chris.pdf.
- Thorncroft, C. D., B. J. Hoskins, and M. E. McIntyre, 1993: Two paradigms of baroclinic-wave life-cycle behaviour. *Quart. J. Roy. Meteor. Soc.*, **119**, 17–55, <https://doi.org/10.1002/qj.49711950903>.
- Torn, R. D., J. S. Whitaker, P. Pegion, T. M. Hamill, and G. J. Hakim, 2015: Diagnosis of the source of GFS medium-range track errors in Hurricane Sandy (2012). *Mon. Wea. Rev.*, **143**, 132–152, <https://doi.org/10.1175/MWR-D-14-00086.1>.
- Wang, Z., W. Li, M. S. Peng, X. Jiang, R. McTaggart-Cowan, and C. A. Davis, 2018: Predictive skill and predictability of North Atlantic tropical cyclogenesis in different synoptic flow regimes. *J. Atmos. Sci.*, **75**, 361–378, <https://doi.org/10.1175/JAS-D-17-0094.1>.
- Wilks, D. S., 2016: “The stippling shows statistically significant grid points”: How research results are routinely overstated and overinterpreted, and what to do about it. *Bull. Amer. Meteor. Soc.*, **97**, 2263–2273, <https://doi.org/10.1175/BAMS-D-15-00267.1>.